Journal of Wind Engineering & Industrial Aerodynamics 249 (2024) 105749

Contents lists available at ScienceDirect

Journal of Wind Engineering & Industrial Aerodynamics

journal homepage: www.elsevier.com/locate/jweia

Comparison of measured and LES-predicted wind pressures on the Space Needle

John Hochschild [*], Catherine Gorlé

Stanford University, Y2E2 Building, 473 Via Ortega, Stanford, CA, 94305, United States of America

ARTICLE INFO

Keywords:
Full-scale measurements
Field measurements
Large-eddy simulations
Wind loading

ABSTRACT

The majority of wind damage is to building envelope components. Large eddy simulations (LESs), which can predict flow fields at high resolution, have significant potential for analyzing component loads. This study aims to (1) demonstrate that LESs can elucidate flow phenomena behind peak pressure loads, and (2) quantitatively compare LESs to full-scale measurements performed on the roof of the 184 m tall Space Needle. The simulations revealed unsteady flow features responsible for pressure signals observed in separation regions and shear layers. Furthermore, predictions for fluctuation pressure coefficients were quantitatively representative of field data. The main discrepancy observed was a more pronounced variability of measured, compared to simulated, shear layer peak pressures. Detailed measurements of the incoming wind field would be needed to further investigate this discrepancy. The results demonstrate the value of joint field measurements and LESs for studying wind effects.

1. Introduction

In 2022, extreme wind events caused $150 billion in damage to buildings and infrastructure in the U.S. alone (National Centers for Environmental Information (NCEI), 2023). The majority of damage from extreme wind events is to the building envelope (cladding) rather than its structure (Sparks et al., 1994; Williams and Kareem, 2003). When the envelope fails, rain ingress can cause damages to be magnified ninefold (Sparks et al., 1994). Additionally, cladding failures often lead to internal pressurization, which drives further damage (Minor, 2005; Ouyang and Spence, 2019).

Currently, wind loads on building envelopes are estimated either using building codes and standards, which are based on wind tunnel pressure measurements on canonical building shapes, or using dedicated wind tunnel measurements for the specific building under consideration. There are two important limitations to this approach. First, it is assumed that peak pressures measured on small-scale wind tunnel models are representative of those experienced by full-scale buildings. Previous studies comparing wind loads measured at model- and full-scale on low-rise structures have consistently found peak pressures to be underestimated at model-scale (Richardson and Surry, 1991; Richardson et al., 1997; Okada and Ha, 1992; Liu et al., 2009; Cochran and Cermak, 1992; Ho et al., 2003). The discrepancies are attributed to differences in the approach turbulent wind fields as well as to the smaller turbulent scales being suppressed at lower Reynolds numbers (Re) (Richardson et al., 1997; Hagos et al., 2014; Okada and Ha, 1992; Tieleman, 2003; Morrison et al., 2011). Both approach flow and Re effects can be expected to also occur on high-rise buildings; however, there is a lack of data to support comparing full- and model-scale loads on high-rise buildings. Second, there is uncertainty in wind tunnel estimates of peak wind loads on envelope elements because limited pressure tap resolutions prohibit direct calculation of area-averaged cladding loads. Assumptions in the form of interpolation and time-filtering have to be made, potentially introducing significant errors in load estimates, especially at critical locations near facade edges and corners (Amerio, 2018; Pomaranzi et al., 2022).

The use of computational fluid dynamics (CFD) may offer a solution to these limitations: the simulations can be performed at full-scale to obviate disparities due to scaling, sensitivities to inflow conditions can be quantified, and the resolution of the pressure data is limited only by the computational grid. Additionally, the ease of visualizing flow at any point within the domain enables engineers to better understand the flow phenomena behind the wind pressure results. Furthermore, an increasing number of studies have successfully validated large-eddy simulation (LES) predictions for peak wind pressure coefficients against wind tunnel data (Ciarlatani et al., 2023; Lamberti et al., 2020; Giangaspero et al., 2022; Elshaer et al., 2016). These studies indicate that there are two main requirements for LES to accurately predict peak wind pressure loads measured in wind tunnel experiments: (1) the statistics of the turbulent wind field at the building location should

---

[*] Corresponding author.
E-mail addresses: john.hochschild@us.af.mil (J. Hochschild), gorle@stanford.edu (C. Gorlé).

https://doi.org/10.1016/j.jweia.2024.105749
Received 23 October 2023; Received in revised form 20 April 2024; Accepted 20 April 2024

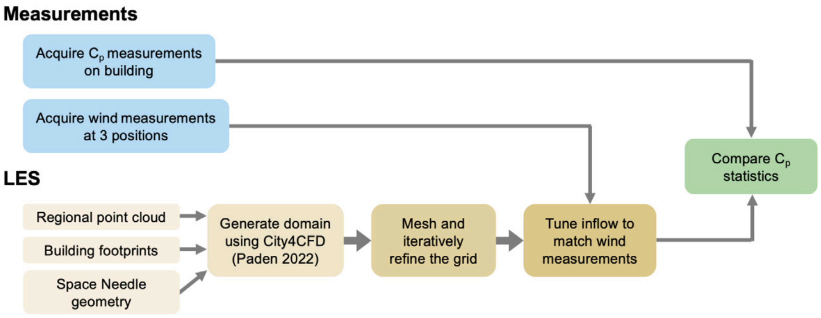

Fig. 1. Flowchart showing the methodological process for both measurements and simulations.

match the experimental flow conditions, and (2) a sufficiently fine grid resolution has to be employed.

The objective of this study is to further demonstrate the potential of CFD for analyzing wind pressure loads by (1) using LES results to elucidate the flow physics that cause specific pressure patterns on a building and (2) quantitatively comparing LES results for fluctuation wind pressure coefficient statistics on a high-rise building to full-scale pressure measurements. To achieve our objective, we use the full-scale data from a measurement campaign that deployed absolute pressure sensors at 10 positions on the sloped roof of the Space Needle, a 184 m tall observation tower in Seattle (Hochschild and Gorlé, 2024). A custom data logging system enabled the sensors to remain on the building for months at a time, gathering pressure time series over a range of wind conditions. The post-processed pressure measurements provide the statistical moments and peak values of the fluctuation pressure coefficient C'_p. A set of LESs was designed to obtain predictions of the same C'_p statistics. The set-up of the simulations carefully considered two aspects that have been shown to be essential for accurate wind pressure predictions: the definition of the turbulent wind conditions, and the grid resolution of the simulations. To represent the range of wind conditions measured during the field measurement, three LESs with different inflow conditions are performed. The simulations are then post-processed to assess the overall flow pattern and the pressure distribution on the Space Needle roof, and detailed flow visualizations are performed to identify the origin of specific patterns in the fluctuation pressure statistics. Subsequently, quantitative comparison of the C'_p statistics obtained from the simulations is performed to demonstrate the predictive capability of LES and potential reasons for difference observed are investigated by analyzing specific measurement and LES time series.

The remainder of this paper is organized as follows. Section 2 describes the methods, summarizing the field measurements and detailing the setup of the LESs. Section 3 presents the LES results, including the overall analysis of the flow and pressure patterns and the quantitative comparison of the wind pressure coefficient statistics. Section 4 summarizes the conclusions of the study.

2. Methods

This section first summarizes the full-scale measurement data and then provides a detailed description of the computational methods. The methods are summarized in the flowchart in Fig. 1.

2.1. Experimental data set

The full-scale data used in this study was obtained from a measurement campaign that is described in detail in Hochschild and Gorlé (2024). In the following we briefly summarize the sensors used and we introduce the quantities of interest to be compared to the LES results.

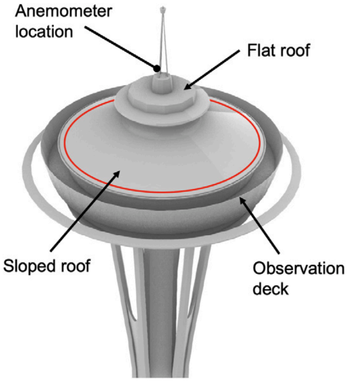

Fig. 2. Space Needle, with sloped roof perimeter along which sensors were deployed indicated in red.

2.1.1. Measurement equipment

The sensor network was made up of novel wireless absolute pressure sensing motes, where each mote has a custom data-logger and three Bosch Sensortec BMP388 sensors (BMP, 2018). With only 1.7 Pa RMS noise and low long-term drift, this sensor is able to measure pressure coefficients C_p within ± 0.1 at relatively low windspeeds ($U > 10$ m/s). The custom housing is low-profile and unobtrusive to minimize aerodynamic interference with the measurements. To detect potential interference, each mote has three pressure ports, positioned on different faces, such that the post-processing routine can exclude measurements during which the three sensors recorded different values. The motes gathered data at 10 distinct positions around the perimeter of the Space Needle's sloped roof (see Fig. 2), about 30 cm from the edge. Because of the circular shape of the building, the measurements are presented as a function of the relative angle of the sensor along the perimeter of the roof, where the 0° angle is defined as the most upstream point given the mean wind direction during the specific measurement period.

In addition to the pressure sensors, three ultrasonic anemometers were installed to characterize the wind incident on the building. One was installed at the top of the Space Needle and two were installed on the roof of the Pacific Science Center (PacSci), a mid-rise building about 150 m upstream of the Space Needle.

2.1.2. Quantities of interest and post-processing methods

The analysis presented in this paper focuses on statistics of the fluctuation pressure coefficient C'_p:

$$C'_p(t) = \frac{P(t) - \overline{P}}{\frac{1}{2}\rho\overline{U}^2}, \tag{1}$$

where $\overline{P}$ is the time-average of the pressure signal $P(t)$, ρ is the density, and $\overline{U}$ is the time-average of the freestream velocity at building height. This wind speed is obtained by correcting the wind speed measured by

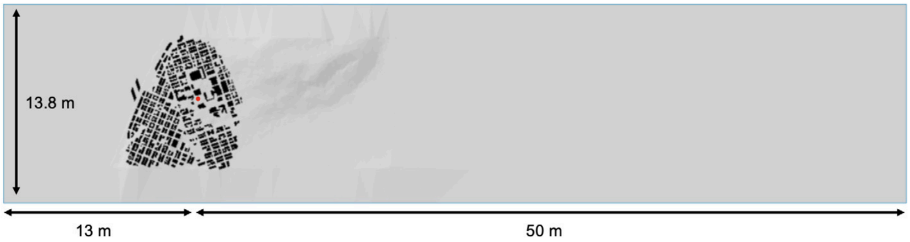

Fig. 3. Top view of computational domain, with surrounding buildings in black and the Space Needle in red. Flow is left to right.

the anemometer installed at the top of the Space Needle to remove the influence of the building geometry. The correction factor is obtained from the LES, which showed a 32% acceleration of the flow measured at the anemometer position relative to the freestream velocity at building height.

The reason for focusing the analysis on C'_p is twofold. First, the calculation of C'_p is not affected by potentially significant uncertainty in the measurement of the reference pressure required to calculate the standard pressure coefficient (Hochschild and Gorlé, 2024). Second, it has been demonstrated that the mean pressure coefficient is generally well predicted by LES, since the mean value is less sensitive to both the numerical modeling choices and the turbulence characteristics in the incoming wind.

The specific C'_p statistics of interest are the second, third, and fourth moments of $C'_p(t)$, i.e. the root-mean-square $C_{p,rms}$, skewness $C'_{p,skew}$, and kurtosis $C'_{p,kurt}$, respectively. In addition, we will consider the minimum peak value $C'_{p,min}$ and the peak factor g, which is the ratio of $C'_{p,min}$ to $C_{p,rms}$. Because the incoming wind field during the measurements is non-stationary over longer time scales, the measured time series are divided into 10-min windows and statistics are calculated for each window.

The minimum peak fluctuation values $C'_{p,min}$ are estimated from an extreme value analysis. The time series of C'_p is divided into 16 windows, and the peak value from each window is recorded. Assuming a type I (Gumbel) extreme value distribution for the peak samples, the peak values with a non-exceedance probability of 78% are then given by $m + 0.636\sigma$, where m and σ are the mean and the rms value of the 16 peak values (Cook and Mayne, 1979, 1980). When dividing the 10-min sampling time into 16 windows, the length of each window is less than the minimum window length $T_{target} = 10$ minutes suggested by Cook and Mayne. The values are therefore corrected to account for the actual sampling time T_{actual} as follows (Kasperski, 2003, 2009):

$$C'_{p,min} = m + \left(0.636 + \frac{\sqrt{6}}{\pi} ln \frac{T_{target}}{T_{actual}}\right) \sigma \frac{m}{|m|} \tag{2}$$

The sample time correction factor in Eq. (2) can introduce uncertainty in the estimates, but the non-stationary character of the wind precludes the use of longer time series.

As noted in Section 2.1.1, the measurement post-processing routine excludes measurements that might be affected by aerodynamic interference induced by the mote shape. When the ranges of $C_{p,rms}$ and $C'_{p,min}$ measured by the three sensors on a single mote exceed certain threshold values, the 10-min window was excluded from the analysis. In this study, we defined the acceptable ranges to be 0.04 for $C_{p,rms}$ and 0.4 for $C'_{p,min}$.

2.2. Computational methods

Large-eddy simulations of the Space Needle and its surroundings were performed using the CharLES solver. This section presents the governing equations and numerical methods, the computational domain and mesh, and the boundary conditions used for the simulations.

2.2.1. Governing equations

In LES, turbulence at the larger scales is resolved by solving the filtered Navier–Stokes equations. The filtering breaks each instantaneous flow variable into a filtered and a subgrid component, e.g., $u_i = \tilde{u}_i + u'_i$ for the velocity components, and the sub-filter turbulent scales are modeled using a subgrid model. For the simulations in this study we use the low-Mach isentropic version of Cadence Systems Design's CharLES solver (Cadence Design Systems, 2023). CharLES is a finite volume solver with an automated body-fitted meshing technique based on 3D-clipped Voronoi diagrams. This approach results in isotropic, polyhedral-type cells that are highly effective for the high-fidelity simulation of turbulent flows. The solver has previously been validated for the assessment of wind loading on a high-rise building wind tunnel model (Ciarlatani et al., 2023). The filtered continuity, momentum, and state equations are given by:

$$\frac{\partial \tilde{\rho}}{\partial t} + \frac{\partial \tilde{\rho}\tilde{u}_i}{\partial x_i} = 0 \tag{3}$$

$$\frac{\partial \tilde{\rho}\tilde{u}_i}{\partial t} + \frac{\partial \tilde{\rho}\tilde{u}_i\tilde{u}_j}{\partial x_j} = -\frac{\partial \tilde{p}}{\partial x_i} + \frac{\partial}{\partial x_j}\left[(\mu + \mu_{SGS})\left(\frac{\partial \tilde{u}_i}{\partial x_j} + \frac{\partial \tilde{u}_j}{\partial x_i} - \frac{2}{3}\delta_{ij}\frac{\tilde{u}_k}{x_k}\right)\right] \tag{4}$$

$$\tilde{\rho} = \frac{1}{c^2}\left(\tilde{p} - p_{ref}\right) + \rho_{ref} \tag{5}$$

where $\tilde{\rho}$ is filtered density, ρ_{ref} is reference density, p_{ref} is reference pressure, c is the speed of sound, μ is the viscosity of air, and the subgrid viscosity μ_{SGS} represents the effects of the subgrid scales on fluid motion. The subgrid viscosity is modeled using the Vreman model (Vreman, 2004).

2.2.2. Computational domain

Fig. 3 shows a top-view of the computational domain, which includes the Space Needle and its surroundings. In the simulations, the domain was scaled down by a factor of 1:200. The dimensions indicated in Fig. 3 are provided at this reduced scale, with the Space Needle height $H = 0.92$ m, and the diameter of the circular top section $D = 0.186$ m. A potential drawback of the reduced scale is that Reynolds number effects might occur. However, the turbulent inflow reduces the typical values for the critical Reynolds number below which these effects occur. The benefit of the reduced scale is that the near-wall grid can be sufficiently fine to use a no-slip boundary condition. At full-scale, the boundary layer on the sloped roof would inevitably be under-resolved and the need to use wall modeling could introduce inaccuracies in the solution. As such, the benefits of using the reduced scale can be assumed to outweigh the drawbacks; comparison between the LES results and the data in Section 3 will support verifying this assumption.

The simulation is performed for the dominant wind direction observed during the full-scale measurement campaign, i.e. $\theta = 200°$. Because of the building's rotational symmetry and the absence of neighboring high-rise buildings, the pressures predicted along the circumference of the roof for this wind direction are independent of the wind direction. As a result, the simulation for the dominant wind direction can be compared to all 10-min field measurement periods by presenting the data as a function of the relative position of the pressure probe or sensor with respect to the incoming wind.

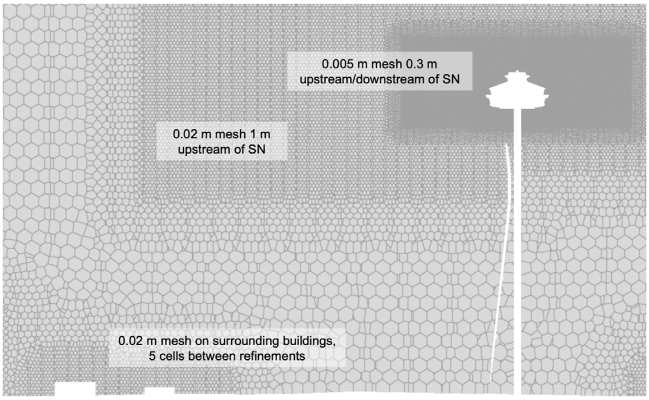

Fig. 4. Detail of mesh near the Space Needle and immediately surrounding buildings, with refinement details annotated.

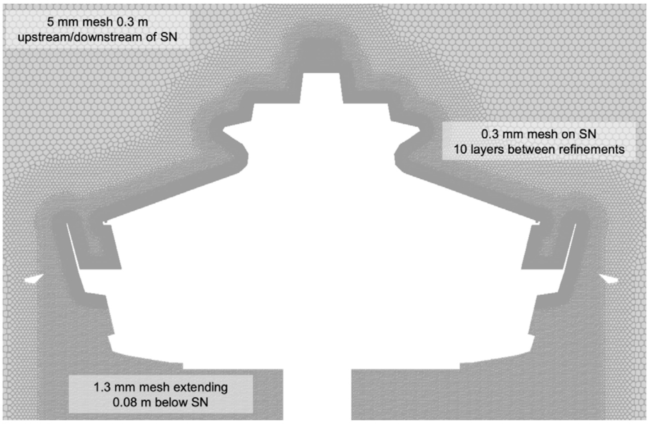

Fig. 5. Detail of mesh around the Space Needle roof, with refinement details annotated.

The domain extends 13 m upstream of the building, with the terrain meeting Elliott Bay 4 m upstream of the Space Needle. Downstream of the building, the terrain is included for 13 m followed by 37 m of flat ground. The domain extends 6.9 m laterally on either side from the Space Needle and is 30 m tall. The terrain is flattened near the sides of the domain to prevent perturbations due to sharp corners near boundaries. The domain height and length allow space for a sponge region at the top and the outlet to avoid reflection of acoustic waves.

Included in the domain are all upstream buildings, and downstream buildings up to $3H$ from the Space Needle. In Fig. 3, the surrounding buildings are black and the Space Needle is red. The geometry of surrounding buildings was prepared from footprint and pointcloud data using City4CFD (Paden et al., 2022). The Space Needle geometry is resolved with high detail, as shown in Fig. 2. Railings, light fixtures, and ducts at the flat roof level are not included since flow disturbances due to these features are negligible at the full-scale measurement locations.

2.2.3. Computational mesh

The mesh is generated using Cadence's Stitch tool, which generates an unstructured Voronoi mesh. Figs. 4 and 5 show images of the mesh near the Space Needle, detailing the different refinement zones in the computational domain. The extent of the different refinement zones and the grid resolutions in each zone were determined by running simulations with gradually refined meshes and observing how much quantities of interest varied. Between the mesh that was ultimately used (19 million cells) and a finer version (with 42 million cells), the mean change in $C_{p,rms}$ around the roof perimeter is 0.01 with a standard deviation of 0.01. Similarly, the mean change in $C'_{p,min}$ is 0.24 with a standard deviation of 0.20. Because the QoIs changed minimally with refinement, we decided the mesh was sufficiently refined. The final mesh used for the simulations presented in this paper contains a total of 19 million cells. The background grid size, used in the upper and most downstream regions of the domain is equal to 0.64 m, while the minimum cell size on the building is 0.31 mm (equivalent to 620 cells per diameter or 6 cm at full-scale).

2.2.4. Boundary conditions

On the lower boundary representing the water and the terrain a logarithmic rough-wall wall function is used to support the logarithmic mean velocity profile imposed at the inlet boundary. The roughness length specified for the water is 5×10^{-6} m, equivalent to 1 mm at full-scale. The roughness length specified for the terrain is 0.005 m, equivalent to 1 m at full-scale. With the finest mesh, the grid resolution around the Space Needle results in a mean $y+$ value on the sloped roof equal to 3.2, which we consider to be low enough to not require a wall model and instead use a no slip boundary condition. This no slip boundary condition is also applied to the surrounding buildings. The sensitivity of the results to the wall treatment was determined to be negligible by also performing a simulation with an algebraic wall function boundary condition on the Space Needle.

A slip wall (zero-stress) boundary condition is used at the top and sides of the domain. A non-reflecting outflow condition is imposed at the outlet. At the inlet boundary, we impose a turbulent velocity field that produces a logarithmic mean velocity profile and turbulence statistics representative of a neutral surface layer over water. The turbulent velocity field is generated artificially using a divergence-free digital filter method (Xie and Castro, 2008; Kim et al., 2013). The digital filter is used in combination with an acoustic subgrid scale sponge. The sponge is applied in a region that extends approximately two turbulent length scales downstream from the inlet, and damps high amplitude, short wavelength acoustic pressure fluctuations that are artificially introduced by the digital filtering turbulence generation. The artificially generated turbulence imposed at the inlet tends to decay within the computational domain (Keating et al., 2004; Jarrin et al., 2009). Hence, the input parameters for the digital filter method were adjusted to ensure the resulting flow conditions near the Space Needle were representative of the wind conditions during the field measurements. This process is discussed in detail in Section 2.2.5.

2.2.5. Inflow input parameters and resulting flow conditions

The implementation of the digital filter method used in the simulations presented in this paper first imposes the mean neutral surface layer logarithmic velocity profile at the inlet plane:

$$U = \frac{u_*}{\kappa} ln\left(\frac{y}{y_0}\right)$$

The von Kármán constant $\kappa = 0.41$ and the roughness length $y_0 = 5 \times 10^{-6}$ m for the water surface at the inlet. The friction velocity is found by imposing $U = 15$ m/s at building height, yielding $u_* = 0.5$ m/s. This results in a Reynolds number of 180,000 based on the roof diameter and windspeed at roof height.

Next, a fluctuating velocity field that is spatially and temporally coherent is generated using a digital filter (Xie and Castro, 2008) and added to the mean velocity profile just downstream of the inlet. To reduce computational cost, this fluctuating velocity field is generated over a subsection of the inlet measuring 2.5 m high by 5 m wide. The field is generated on a uniform grid of 25 × 50 cells (i.e. grid spacing $L_{y,z} = 0.1$ m) and interpolated to the Voronoi cell centers. The resulting instantaneous velocity is then corrected by the correction step in the solution algorithm to satisfy continuity and reduce artificial pressure fluctuations, similar to the approach of Kim et al. (2013).

The digital filter method requires inputs for the Reynolds stresses, the streamwise time scales, and the spanwise and vertical length scales

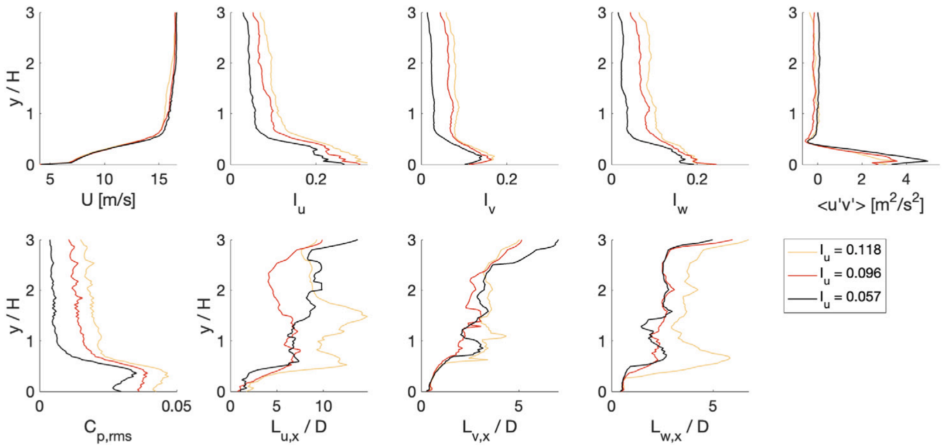

Fig. 6. Case comparison of vertical profiles of velocity, turbulence intensities, shear stress, RMS pressure, and length scales $1H$ upstream of the Space Needle.

Table 1
Nominal target conditions and three sets of optimized inflow input parameters used for Space Needle simulations. $\overline{U}$ is the mean wind speed at the anemometer and D is the roof diameter. L_y and L_z are assumed equal for all three velocity components.

Inflow parameter	Target values for nominal I_u	Input values optimized for nominal I_u	Input values optimized for high I_u	Input values optimized for low I_u
I_u	0.11	0.11	0.11	0.055
I_v	$0.25I_u$	$1.0I_u$	$1.0I_u$	$0.125I_u$
I_w	$0.64I_u$	$2.5I_u$	$2.5I_u$	$0.32I_u$
$\frac{L_{u,x}}{D}$	7.02	7.02	14.04	7.02
$\frac{L_{v,x}}{D}$	$0.46\frac{L_{u,x}}{D}$	$0.46\frac{L_{u,x}}{D}$	$0.46\frac{L_{u,x}}{D}$	$0.46\frac{L_{u,x}}{D}$
$\frac{L_{w,x}}{D}$	$0.2\frac{L_{u,x}}{D}$	$0.2\frac{L_{u,x}}{D}$	$0.2\frac{L_{u,x}}{D}$	$0.2\frac{L_{u,x}}{D}$
$\frac{L_y}{D}$	$\frac{L_{v,x}}{D}$	$\frac{L_{v,x}}{D}$	$\frac{L_{v,x}}{D}$	$\frac{L_{v,x}}{D}$
$\frac{L_z}{D}$	$\frac{L_{w,x}}{D}$	$\frac{L_{w,x}}{D}$	$\frac{L_{w,x}}{D}$	$\frac{L_{w,x}}{D}$

at the inflow. Since the flow imposed at the inflow boundary will evolve as it moves downstream, these inputs were defined to ensure that the flow field generated at the Space Needle location is representative of the flow conditions recorded by the anemometers during the field measurements. Because the field measurement data revealed significant variability in the incoming wind conditions (Hochschild and Gorlé, 2024), we defined three sets of input parameters to perform three different simulations representative of the observed variability in the field measurements.

We followed a two-step process for defining the three sets of input parameters:

1. Perform a simulation with the input velocity statistics representing a nominal target condition and record the decay in turbulence between the inlet and the anemometer location near the Space Needle.
2. Optimize the inputs for the $v'v'$ and $w'w'$ stresses and the $L_{u,x}$ length scale to achieve the three sets of input parameters that result in the desired range of turbulence intensities near the Space Needle, similar to the process proposed in Lamberti et al. (2018).

Table 1 summarizes both the nominal target condition and the three sets of input parameters resulting from the optimization process. The nominal target condition was defined based on the anemometer measurements for the streamwise turbulence intensity $I_u = \sqrt{\overline{u'u'}}/\overline{U}$, and corresponding non-dimensional streamwise length-scale $L_{u,x}/D = T_{u,x}\overline{U}/D$. The vertical $I_v = \sqrt{\overline{v'v'}}/\overline{U}$ and spanwise $I_w = \sqrt{\overline{w'w'}}/\overline{U}$ turbulence intensities and other length scales are defined using empirical relationships. All input values were imposed constant over the height of the domain and then adjusted to realistic profiles further downstream due to the interaction with the terrain and buildings. Fig. 6 shows the mean velocity profiles, turbulence intensities, shear stress, and non-dimensional length scales $1H$ upstream of the Space Needle obtained using the three optimized inflow conditions. The profiles are labeled using the recorded turbulence intensity at the location of the Space Needle roof anemometer, and this labeling will be used when presenting results throughout the remainder of this paper. The profiles in Fig. 6 reflect the development on an internal boundary layer when the terrain changes from water to land, which involves changes in both the slope and the roughness characteristics of the surface. The plots represent the flow conditions to which the Space Needle is subjected, and these profiles should therefore be the target profiles in any studies intending to reproduce or compare to the simulation results presented in this paper.

To conclude this section, Fig. 7 shows that the three sets of simulations provide a realistic representation of the range of flow conditions observed during the field measurements by comparing the LES velocity statistics at the three anemometers to the measured data. The markers show results for all three LES cases. The velocity statistics agree very well between the measurements and the LES: the LES cases fall within the measured ranges for turbulence intensities and length scales, and the relative positions are mostly consistent across the different statistics.

2.2.6. *Numerics and quantities of interest*

The governing equations are discretized with a second-order central scheme in space and a second-order backward difference scheme in time (Ambo et al., 2020). CharLES' multigrid solver is used to allow running the simulation with a maximum CFL number on the order of 3, which corresponds to a timestep of 2.5×10^{-5} s. After the initial transient has disappeared, the simulations are run to obtain 18 s of pressure and velocity time series, which corresponds to 1 h full-scale time.

Pressure probes are sampled every 16 timesteps, resulting in a full-scale equivalent sampling frequency equal to the measurement f_s = 12.5 Hz. C_p' statistics are calculated as introduced in Section 2.1.2, with the correction factor in Eq. (2) adjusted to account for the longer sampling time. The longer time series obtained from the LESs will also be used to assess the uncertainty related to the use of 10-min time series from the experiments.

3. Results

This section first presents velocity field visualizations and an analysis of the velocity predictions at the anemometer location for the simulations with the turbulence intensity of 9% at the anemometer

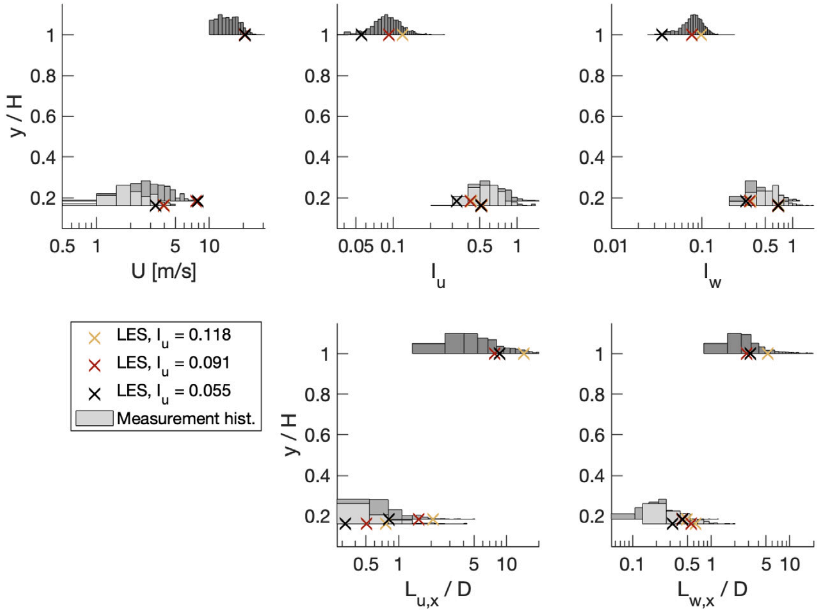

Fig. 7. Velocity, streamwise/spanwise turbulence intensities and length scales as measured by the anemometers (histograms) and in the LES (X markers).

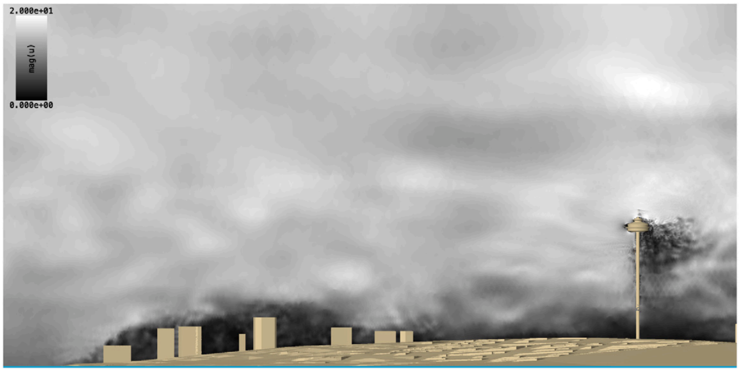

Fig. 8. Instantaneous velocity in the domain for the nominal case.

location. Next, these simulations are used to analyze the pressure fluctuations on the sloped roof, plotting contours of C_p' statistics and connecting specific flow patterns to these results. Subsequently we compare the LES predictions for all turbulence intensities to the field measurement data, considering C_p' statistics as well as time series and spectra from a few specific 10-min measurement periods.

3.1. Visualization and analysis of the velocity field

3.1.1. Velocity contour plots

Fig. 8 shows a velocity contour snapshot in the computational domain, showing the Space Needle and surrounding buildings. The plot qualitatively visualizes the effect of the upstream terrain and buildings on the surface layer wind flow. Fig. 9 shows more detailed time-averaged and instantaneous contours of velocity around the Space Needle top. The plots indicate a stagnation region upstream, and a first flow separation at the top of the glass panels surrounding the observation deck. The flow then reattaches along the sloped roof and separates again further downstream due to the presence of the cylindrical extrusion supporting the upper deck.

3.1.2. Analysis of velocity signal at rooftop anemometer

The velocity contour plots in Fig. 9 indicate that the flow on the upper deck, where the anemometer is located, is accelerated compared to the freestream conditions at roof height. The LES results are therefore used to determine the ratio of mean freestream velocity over mean anemometer velocity, such that the freestream velocity required to calculate C_p' can be recovered from the anemometer measurements. LES velocity time series from the freestream $1H$ upstream and at the rooftop anemometer location are compared in Fig. 10. The plot clearly shows how the rooftop anemometer data lags the freestream probe data upstream, but with increased amplitude. The ratio of mean freestream velocity over mean anemometer velocity was determined to be 0.76 for all three turbulence intensity cases. The plot also shows that the time series at the anemometer location reveals smaller scale fluctuations due to the locally refined mesh. This finding is reflected in the spectra for both the streamwise and spanwise velocity components, shown in Fig. 11. The figure also plots the velocity spectra obtained from the field measurements, confirming that the turbulence in the LES velocity field is representative of the full-scale conditions.

In Section 2.1.2, we introduced that data from measurements for all wind angles can be presented in a single plot due to the building's rotational symmetry. Since the presence of the spire geometry on the rooftop could disturb the rotational symmetry at the anemometer location, we also verified that the velocity scale factor has only a minor change with the wind direction. We found that the velocity ratio was within 5% of 0.76 for 97% of data measured during the experiments and we will therefore treat the scale factor as constant across our data.

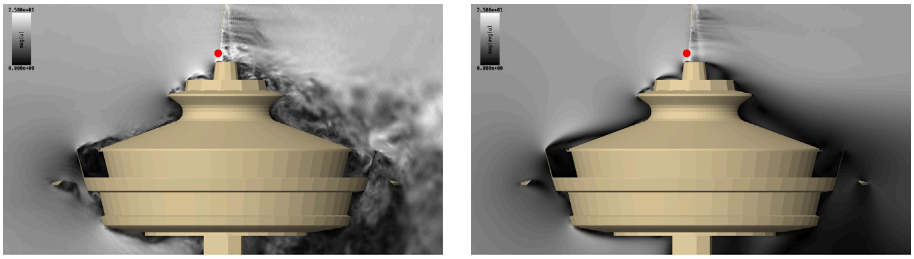

(a) Instantaneous (b) Time-averaged

Fig. 9. Velocity contours in the computational domain near the Space Needle roof for the nominal case. The red markers indicate the rooftop anemometer location when wind is from the dominant direction.

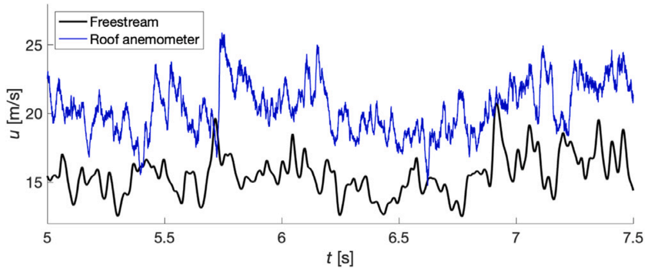

Fig. 10. LES velocity time series of freestream $1H$ upstream at roof height and rooftop anemometer location.

3.2. LES-based analysis of C_p' statistics on the sloped roof

3.2.1. Contour plots of C_p' statistics

Contours of C_p' statistics on the roof are shown for the nominal case in Fig. 12. The upper left plot shows the mean streamwise velocity on the roof to highlight regions of flow separation as those with negative mean velocity. As observed in the velocity contour plots in Fig. 9, there are two separation regions: a windward separation region caused by the flow separating over the glass wall of the observation deck below, and a leeward separation region caused by the raised central roof geometry. These zones, as well as the shear layers that form either side of the leeward cylinder wake, are annotated on the diagram at bottom left in Fig. 12.

The windward separation region shows the highest $C_{p,rms}$ values, while the two shear layers between the leeward separation region and the attached flow on the sides show the most negative $C_{p,min}'$. The fact that the region with the highest $C_{p,rms}$ does not produce the most negative $C_{p,min}'$ can be explained by considering the skewness and kurtosis plots. Near the upstream edge, the skewness takes on positive values, indicating that positive fluctuations occur more frequently than negative fluctuations, thereby resulting in more moderate $C_{p,min}'$ values. In contrast, the shear layers are characterized by a strongly negative skewness and a high kurtosis, thereby producing strongly negative $C_{p,min}'$ values. These general observation are consistent with previously published observations from the field measurements (Hochschild and Gorlé, 2024). In the remainder of this section, we first use the LES to identify the flow patterns responsible for the difference between the fluctuation characteristics in both flow regions. Subsequently, we present the quantitative comparisons between the LES results and the field measurements in Sections 3.3 and 3.4.

3.2.2. Origin of positive skewness in the windward separation region

The positive skewness in the windward separation region is noteworthy because separation regions typically have negatively skewed C_p' distributions. Instead, the LES probes in this region reveal more frequent and greater magnitude positive C_p' fluctuations. A detail of the LES (9% I_u case) time series from the 0° (most windward) perimeter probe near one of these positive peaks is shown in Fig. 13. Along with the time series, the figure shows three contours of instantaneous velocity magnitude at three times. The time series is taken from the probe location denoted by the white X in the images. At time A, the observation deck glass panel below the roof prompts flow separation and a recirculation bubble results in reversed flow on the roof. At time B, we see how the recirculation bubble is reduced in size, and the sign of C_p' changes from negative to positive. Finally, as visualized at time C there is a period of time where the recirculation region is limited to the area above the observation deck opening and so the flow on the windward roof is attached. We therefore see that the positive skewness near the leading edge of the sloped roof is attributed to a significant fluctuation in the size of the separation region originating at the observation deck glass panels.

3.2.3. Origin of negative peak pressures in the shear layers

While the highest $C_{p,rms}$ are observed in the windward separation region, Fig. 12 showed how the most extreme suction pressures are seen in the shear layers that form at the interface between attached and separated flow on the roof's leeward side. Fig. 14 plots a detail of C_p' near a peak with three corresponding snapshots of pressure contours on the building surface (top images) and Q-criterion isosurfaces (Jeong and Hussain, 1995) (bottom images). The images show a vortex of strongly negative pressure passing over the probe location, denoted by the blue X. Images A, B, and C show the vortex before it reaches the probe, passing directly over the probe, and breaking up as it reaches the edge of the roof after being advected past the probe.

3.2.4. Analysis of $C_{p,min}'$ sample time correction

The uncertainty introduced by multiplying by the sampling time correction factor in Eq. (2) is illustrated in Fig. 15. The figure compares $C_{p,min}'$ calculated from the entire 60-min LES time series (x axis) versus the mean and range of $C_{p,min}'$ values obtained from dividing the same 60-min time series into 6 10-min windows (y axis). Each data point represents a probe on the perimeter of the sloped roof. Because the sampling time correction factor is different for the two window lengths, the deviation from the $y = x$ line quantifies the uncertainty associated with this method. Since the mean values follow this line closely, we contend that the sampling time correction results in accurate $C_{p,min}'$ estimates. However, the significant spread of the error bars also shows how individual $C_{p,min}'$ estimates vary significantly when calculated from a shorter time series.

3.3. Comparison of C_p' statistics from LES and field measurement data

Fig. 16 compares measured and LES-simulated $C_{p,rms}$ and $C_{p,min}'$ around the sloped roof perimeter. Each measurement data point represents statistics from a 10-min time series and the LES results from the three alternate inflow cases are shown. The turbulence intensities measured at the rooftop anemometer for these three cases are 0.118, 0.091, and 0.055. Comparing the LES curves with the measurement datapoints, three things can be noted. First, the trends and magnitudes

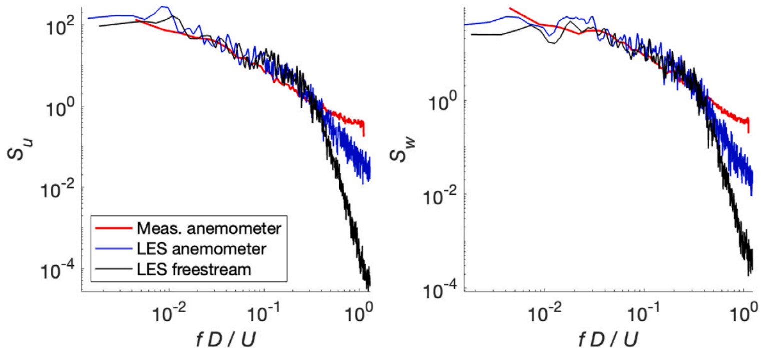

Fig. 11. Comparison of velocity spectra between rooftop anemometer measurements, rooftop anemometer in the LES, and the LES freestream $1H$ upstream at roof height. Frequencies are non-dimensionalized by diameter D and mean velocity U.

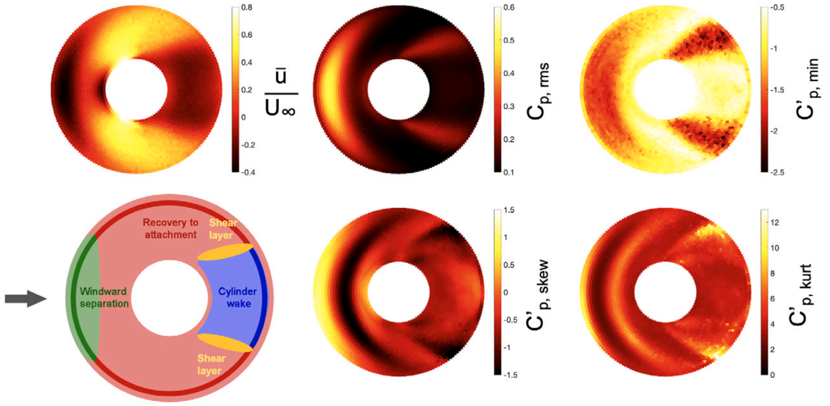

Fig. 12. Contours of pressure coefficient statistics and of mean streamwise velocity on the roof. Bottom left diagram shows the terminology used for flow regions on the roof. Flow is from the left, as denoted by the arrow at bottom left.

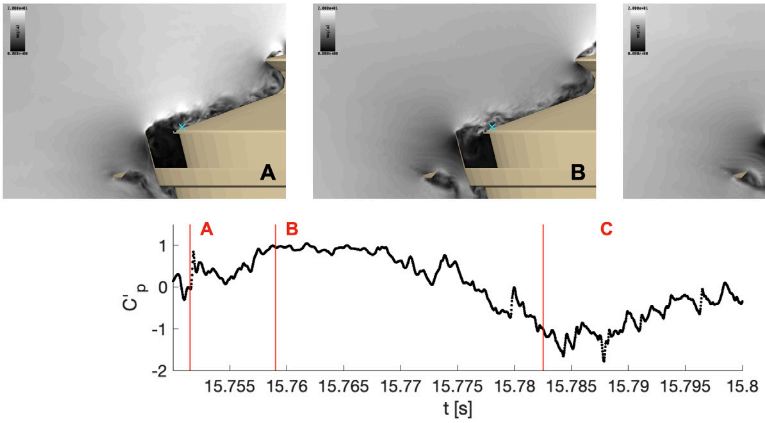

Fig. 13. LES C'_p time series (model scale time) of a probe in the windward separation region with three snapshots showing velocity on a streamwise plane. The probe location at which the time series is taken is denoted by a white X in each image.

of $C_{p,rms}$ and $C'_{p,min}$ around the perimeter of the roof agree very well between LES and measurements. For the higher turbulence intensities both the field measurements and the LES show the highest $C_{p,rms}$ in the windward separation region, but the most negative $C'_{p,min}$ occurs in the leeward shear layers. Second, the effect of the differing upstream turbulence conditions on $C_{p,rms}$ is consistent between the LES and the experiments. In both cases, the upstream turbulence has a much more pronounced effect on $C_{p,rms}$ in the windward region compared to the leeward shear layers and separation region. In the windward region, the LES predicts $C_{p,rms}$ values that are on the higher end of the values recorded in the measurements for corresponding values of I_u. Third, in the two leeward shear layers, the LES $C'_{p,min}$ is consistently representative of the measurements with the most extreme values.

Fig. 17 compares the peak factor magnitude between the measurements and LES. Three similar observations as for Fig. 16 can be made. First, we see good agreement between the three LES runs and the measurements: the LES curves mostly fall in the range obtained from the measurements, and in both cases the highest peak factors occur in the leeward shear layers. The highest value measured for a 10-min window was 16.4 while the LES-predicted maximum was 13.8. These values far exceed the building code's value of 3.4 for a Gaussian signal (of Civil Engineers, 2022), shown by the dashed line on Fig. 17. Second, both the LES and experimental data show a reduced effect of

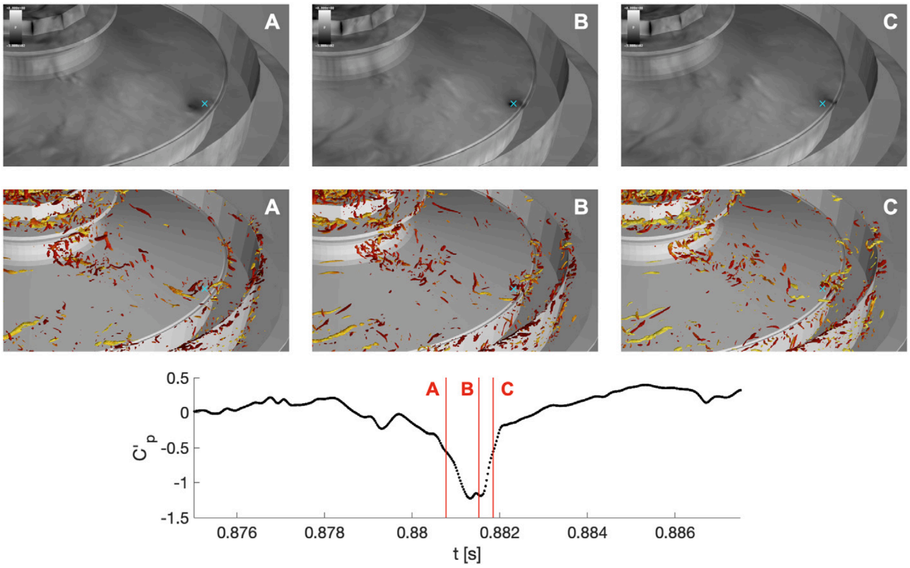

Fig. 14. LES C_p' time series (model scale time) of a probe in the shear layer with three snapshots showing surface pressure on the roof (top images) and isosurfaces of Q-criterion, colored by velocity magnitude (bottom images).

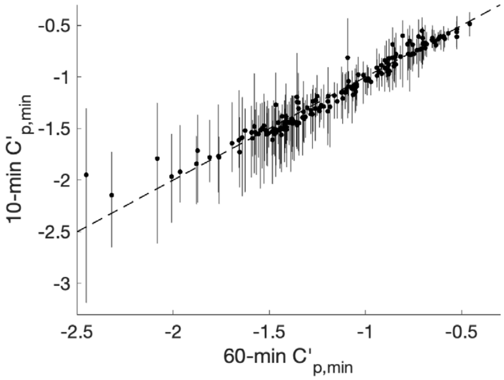

Fig. 15. Comparison of $C_{p,min}'$ calculated based on 10-min versus 60-min window lengths of time series at probes around the perimeter of the sloped roof.

the turbulence intensity recorded at the anemometer on the peak factor. Third, the peak factors predicted in the shear layers are on the higher end of the peak factors calculated from the 10-min measurement time series.

Fig. 18 visualizes the deviation from a Gaussian C_p' signal around the roof's perimeter by plotting the skewness and kurtosis. Again, we point out three observations. First, there is close agreement between the measurements and LES. Considering the skewness, both the measurements and the LES show positive values in the windward separation regions and negative values in the shear layers. Combined with the fact the highest kurtosis values are observed in the shear layers, the change in the sign of the skewness explains why the most negative values for $C_{p,min}'$ occur in the shear layers. Second, the effect of I_u on the skewness and kurtosis is similar in the measurements and simulations. In the windward and attached flow regions the signal becomes more Gaussian as I_u decreases; while in the shear layers and wake the effect of I_u seems reduced. Third, the predictions for the kurtosis in the shear layer represents the highest values measured during the experiment.

In summary, the comparison between LES results and field measurements indicates that the LES correctly reproduces the magnitudes and trends in higher-order C_p' statistics on the sloped roof. The main discrepancies are observed in the shear layers, where the LESs consistently predict the most negative peak values and the highest kurtosis values recorded across all 10-min measurement periods in the field measurements. In the following section we present additional analysis of specific 10-min measurement periods to further investigate this observation.

3.4. Additional analysis of C_p' time series and spectra

The spread of the $C_{p,min}'$ and kurtosis values observed in the shear layers during the field experiments should be assumed to be at least partially caused by a lack of statistical convergence of the estimates based on the 10-min measurement periods. One could improve convergence by averaging the values of a sufficient number of 10-min measurement periods. However, this is only a valid approach if each 10-min period has the same parent distribution for C_p'. There are two reasons why it can be suspected that this is not the case. First, the spread in the data is larger than what would be expected from statistical convergence errors alone. Second, any averaging of data points would ultimately result on the field measurements providing lower $C_{p,min}'$ and kurtosis values than those predicted by the LES.

Fig. 19 presents velocity and C_p' time series for two measurement periods (left two columns) as well as a 10-min full-scale equivalent time period from the 9% Iu LES (rightmost column). The table summarizes the corresponding wind and C_p' statistics. For the measurements, the statistics are calculated for each of the two 10-min measurement windows shown. For the LES, the statistics are calculated for the full 60-min series. In addition, the range (minimum and maximum) obtained from all 6 10-min windows within the full hour are reported. The measurements periods were selected to have different $C_{p,min}'$ estimates, but very similar velocity statistics recorded at the anemometer. Furthermore, both measurement time series were obtained from the same mote and acquired for the same wind direction ($\Delta\overline{\theta} = 0.4°$ between the two). The plot confirms that the two measured wind time series qualitatively look similar and the table quantitatively confirms the streamwise and spanwise turbulence intensities and timescales to also be similar. One could then expect the C_p' time series to have the same parent distribution, but the plot shows that these look quite different: the first (May 16) time series has a lower $C_{p,rms}$ and shows less extreme peak fluctuations compared to the second. This results in less negative $C_{p,min}'$ values.

To provide a more complete picture of the statistics of the time series, Fig. 20 shows the wind and pressure spectra for the time series plotted in Fig. 19. The wind spectra from the two measurement

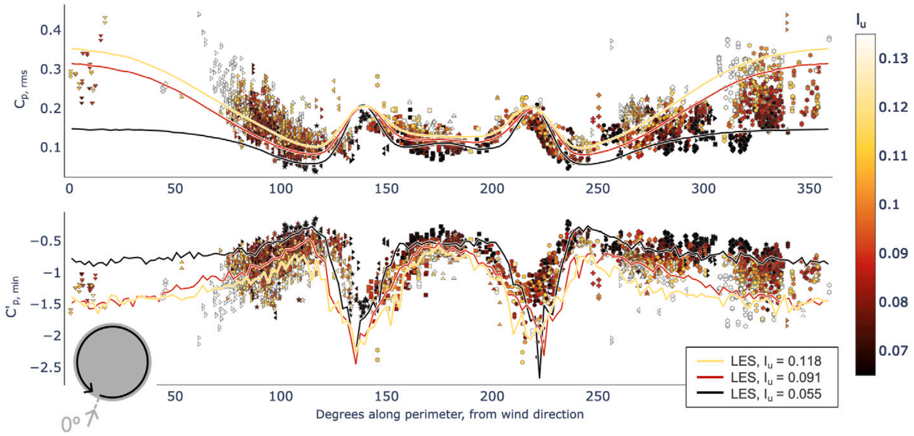

Fig. 16. Measured and simulated $C_{p,rms}$ and $C'_{p,min}$ around the perimeter of the Space Needle's sloped roof. Marker color corresponds to turbulence intensity as measured by the rooftop anemometer and marker shape corresponds to the mote that took the measurement. The meaning of the x-axis is illustrated by the diagram at bottom left.

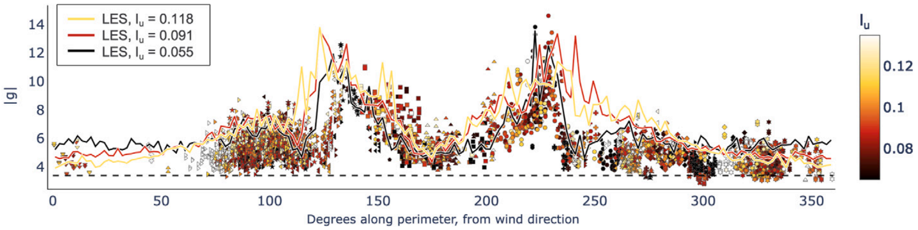

Fig. 17. Peak factor magnitude around the perimeter of the sloped roof, with individual measurement datapoints and results from the three LES cases. The dashed line shows $|g| = 3.4$, the value used by ASCE 7.

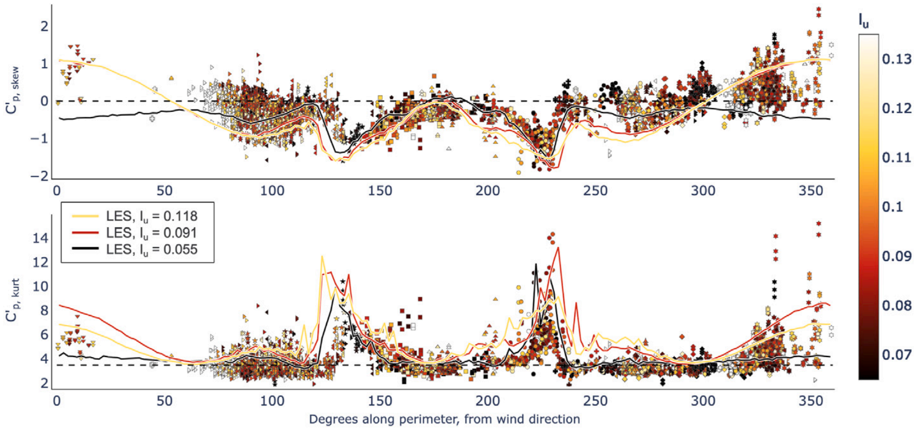

Fig. 18. Skewness and kurtosis around the perimeter of the sloped roof, with individual measurement datapoints and results from the three LES cases (lines).

windows show close agreement, just as we saw in the time series and statistics. The LES velocity spectra reveal slightly more energy at the larger scales and then a steeper decrease in energy towards the smaller scales compared to the measurements. The pressure spectra show how the second (Jun 29) measurement window has increased overall spectral energy in pressure fluctuations in the shear layer despite the similarity of the velocity spectra between the two measurement windows. The spectral energy in the LES more closely represents the second measurement window.

The analysis presented in this section was repeated for other time series that had similar velocity statistics at the anemometer but different $C'_{p,min}$ values in the shear layer. Similarly as for Fig. 19, it was observed that there is a clear difference in the parent distributions of C'_p. We also produced a correlation plot between I_u, I_v, $L_{u,x}/D$, $L_{v,x}/D$, $C_{p,rms}$ and $C_{p,min}$ for all measurement time series recorded in the shear layers. This plot revealed a lack of correlation between the anemometer turbulence intensities or length scales and $C'_{p,min}$; the only correlation observed was between $C_{p,rms}$ and $C'_{p,min}$. Lastly, we ruled out the potential of water interfering with pressure sensing by considering previous rainfall in the analysis.

The additional analysis presented in this section thus confirms that there are differences in the parent distributions of C'_p that cannot be clearly explained by differences in the wind field at the anemometer. It can be hypothesized that there are actual differences in the incoming wind field, but that due to interference effects close to the Space Needle top these differences are not apparent at the rooftop anemometer. This finding indicates the importance of complementing future field measurements of wind pressures with an extensive characterization of the incoming wind field, ideally using a combination of anemometer towers and LiDAR profilers.

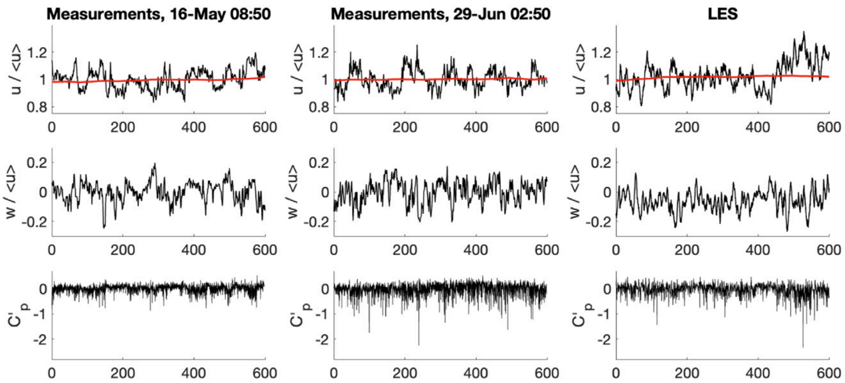

	Measurements, 16-May	Measurements 29-Jun	LES, full time series	LES, 10-min ranges
U [m/s]	12.5	13.2	20.6	[20.2, 21.1]
I_u	0.07	0.07	0.09	[0.083, 0.096]
I_w	0.07	0.08	0.07	[0.068, 0.087]
$L_{u,x}$ / D	3.9	2.9	7.8	[5.8, 12.8]
$L_{w,x}$ / D	2.0	1.6	2.8	[2.1, 3.5]
$C_{p,rms}$	0.14	0.20	0.19	[0.18, 0.19]
$C'_{p,min}$	-1.1	-2.3	-2.3	[-2.7, -1.7]

Fig. 19. Velocity (as measured by rooftop anemometer) and C_p' time series during two 10-min acquisition windows from a mote in the shear layer, compared with the time series at the same location from the 9% I_u LES. The table below gives wind statistics and $C_{p,rms}$, $C_{p,min}'$ values for each window.

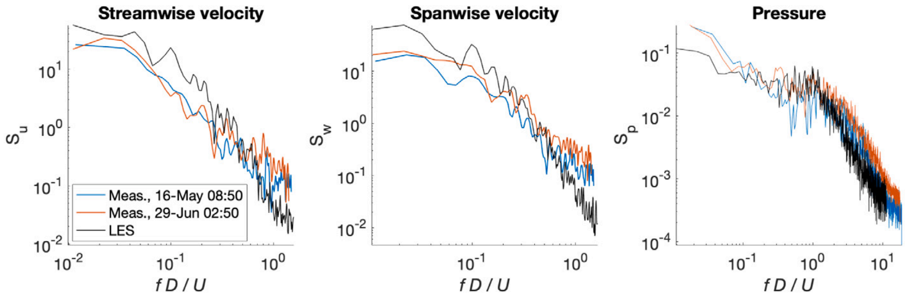

Fig. 20. Streamwise and spanwise and velocity spectra and pressure spectra for the two measurement windows (blue and orange) and the LES (black). Frequency is non-dimensionalized by roof diameter D and mean streamwise velocity U.

4. Summary and conclusions

In this study, we performed large-eddy simulations aimed at reproducing the wind loading phenomena measured during a full-scale pressure measurement campaign on the Space Needle roof (Hochschild and Gorlé, 2024). The goal of the simulations was to (1) elucidate the flow phenomena causing the observed pressure fluctuation statistics, and (2) quantitatively compare the LES and full-scale measurement data.

The simulations were carefully designed in terms of the grid resolution and the inflow boundary conditions. The grid resolution was defined through a mesh sensitivity analysis, gradually refining the mesh until no significant changes in our quantities of interest were observed. Three sets of inflow conditions were optimized to result in velocity statistics that were representative of the range of conditions observed during the field measurements on the Space Needle roof and on upstream mid-rise building roofs. The resulting simulations reproduced the trends observed in the field measurements and analysis of the joint velocity and pressure field enabled identifying the origin of two distinct measurement observations. First, the positive skewness of the pressure in the windward separation region was shown to be caused by a significant fluctuation in the size of the separated flow region, causing occasional periods of attached flow at the sensor locations. Second, highly negative peak pressures in two symmetric leeward regions on the roof were identified to be due to vortical structures in the shear layers caused by flow separation around the cylindrical structure protruding from the center of the roof. In this region, estimated values of the peak factor can be as high as 14, far exceeding the building code's value for a 0.1% probability-of-exceedance in a Gaussian signal (Davenport, 1964).

Quantitative comparison of fluctuation pressure coefficient statistics to the full-scale measurement data confirmed the validity of the LES results. For all statistics the results from simulations largely fell within the range established by the measurements. Furthermore, the three simulations correctly reproduced the expected effect of the turbulence intensity in the incoming wind on the pressure statistics at most sensor locations. The only location where the LESs did not reproduce the full range of values observed in the measurements was in the shear layers. In this region, the LES consistently predicted the most negative peak values (and correspondingly the highest kurtosis values) observed in the measurements. The measurement data indicates significant spread, with only a limited number of measurement periods producing the highly negative peaks predicted by the LES. Analysis of individual 10-min measurement periods indicates that the fluctuating pressure coefficient time series in the shear layer can have significantly different statistical distributions even when the wind conditions measured by the roof anemometer are nearly identical. This observation indicates that there might be differences in the upstream wind that are not reflected in the available anemometer measurements but that do affect the flow in the shear layers.

In conclusion, our study highlights important advantages of using carefully designed LESs and field measurements as complementary methods to wind tunnel experiments to investigate wind loading. First, the ease of flow visualizations based on LES results can provide detailed insight into wind loading phenomena for specific structures. Second, the LESs can provide quantitatively representative predictions for fluctuation pressure coefficients at full-scale, and they provide information at a much higher spatial resolution than possible in experiments. Third, field measurements can be an extremely valuable source of information, eliminating any potential geometrical scaling effects and revealing the variability in wind pressure loads that occurs at full scale.

Our results also reveal two main recommendations for future studies. First, studies should ideally leverage convergence of wind tunnel measurements, LES, and field measurements. The wind tunnel measurements would provide a validation data set under easily reproducible stationary wind conditions, and they would support comparing mean pressure coefficients in addition to fluctuation statistics. Second, field measurements should be complemented with more advanced methods for characterizing the incoming wind field, ideally including LiDAR profilers that can measure mean velocity and turbulence intensity profiles with height. These additions would increase cost and complexity, but our results demonstrate the significant potential value of a thoughtful methodological convergence approach towards improving our understanding and the characterization of wind loads at full scale.

CRediT authorship contribution statement

John Hochschild: Writing – original draft, Methodology, Investigation, Formal analysis. **Catherine Gorlé:** Writing – review & editing, Supervision, Methodology, Conceptualization.

Declaration of competing interest

The authors declare that they have no known competing financial interests or personal relationships that could have appeared to influence the work reported in this paper.

Data availability

Data will be made available on request.

Acknowledgments

This material is based upon work supported by the National Science Foundation, United States under Grant No. (1749610). Any opinions, findings, and conclusions or recommendations expressed in this material are those of the author(s) and do not necessarily reflect the views of the National Science Foundation. Additional support was obtained through an ARUP Global Research Challenge, United States award, and the Stanford Leavell Fellowship, United States program. We are grateful to Melissa Burton and Rubina Ramponi from ARUP for their early guidance on the design of the sensor network. We also extend our gratitude to David Wright for making the Space Needle available for this research work and to Joel Dazey and other Space Needle staff for their support of the project.

References

Ambo, Kei, Nagaoka, Hiroaki, Philips, David A, Ivey, Chris, Brès, Guillaume A, Bose, Sanjeeb T, 2020. Aerodynamic force prediction of the laminar to turbulent flow transition around the front bumper of the vehicle using dynamic-slip wall model LES. In: AIAA Scitech 2020 Forum. p. 0036.

Amerio, L., 2018. Experimental High Resolution Analysis of the Pressure Peaks on a Building Scale Model Facades (Ph.D. thesis). Italy.

2018. BMP388: Digital Pressure Sensor. (BST-BMP388-DS001-01), Bosch Sensortec, Rev. 1.1.

Cadence Design Systems, 2023. Charles, https://www.cascadetechnologies.com/.

Ciarlatani, Mattia Fabrizio, Huang, Zhu, Philips, David, Gorlé, Catherine, 2023. Investigation of peak wind loading on a high-rise building in the atmospheric boundary layer using large-eddy simulations. J. Wind Eng. Ind. Aerodyn. 236, 105408.

of Civil Engineers, American Society, 2022. Minimum Design Loads and Associated Criteria for Buildings and Other Structures. American Society of Civil Engineers.

Cochran, L.S., Cermak, J.E., 1992. Full- and model-scale cladding pressures on the Texas Tech university experimental building. J. Wind Eng. Ind. Aerodyn. 43 (1), 1589–1600, URL https://www.sciencedirect.com/science/article/pii/016761059290374J. International Conference on Wind Engineering.

Cook, N.J., Mayne, J.R., 1979. A novel working approach to the assessment of wind loads for equivalent static design. J. Wind Eng. Ind. Aerodyn. 4 (2), 149–164.

Cook, N.J., Mayne, J.R., 1980. A refined working approach to the assessment of wind loads for equivalent static design. J. Wind Eng. Ind. Aerodyn. 6 (1–2), 125–137.

Davenport, Alan Garnett, 1964. Note on the distribution of the largest value of a random function with application to gust loading. Proc. Inst. Civ. Eng. 28 (2), 187–196.

Elshaer, Ahmed, Aboshosha, Haitham, Bitsuamlak, Girma, El Damatty, Ashraf, Dagnew, Agerneh, 2016. LES evaluation of wind-induced responses for an isolated and a surrounded tall building. Eng. Struct. 115, 179–195.

Giangaspero, Giorgio, Amerio, Luca, Downie, Steven, Zasso, Alberto, Vincent, Peter, 2022. High-order scale-resolving simulations of extreme wind loads on a model high-rise building. J. Wind Eng. Ind. Aerodyn. 230, 105169.

Hagos, A., Filmon, H., Chowdhury, A.G., Yeo, D., 2014. Comparisons of two wind tunnel pressure databases and partial validation against full-scale measurements. J. Struct. Eng. 140 (10), 04014065.

Ho, T.C.E., Surry, D., Morrish, D., 2003. NIST/TTU Cooperative Agreement/windstorm Mitigation Initiative: Wind Tunnel Experiments on Generic Low Buildings. Technical Report, Western University.

Hochschild, John, Gorlé, Catherine, 2024. Design and demonstration of a sensing network for full-scale wind pressure measurements on buildings. Preprint.

Jarrin, N, Prosser, R, Uribe, J-C, Benhamadouche, S, Laurence, D, 2009. Reconstruction of turbulent fluctuations for hybrid RANS/LES simulations using a synthetic-eddy method. Int. J. Heat Fluid Flow 30 (3), 435–442.

Jeong, Jinhee, Hussain, Fazle, 1995. On the identification of a vortex. J. Fluid Mech. 285, 69–94.

Kasperski, M., 2003. Specification of the design wind load based on wind tunnel experiments. J. Wind Eng. Ind. Aerodyn. 91 (4), 527–541.

Kasperski, Michael, 2009. Specification of the design wind load—A critical review of code concepts. J. Wind Eng. Ind. Aerodyn. 97 (7–8), 335–357.

Keating, Anthony, Piomelli, Ugo, Balaras, Elias, Kaltenbach, Hans-Jakob, 2004. A priori and a posteriori tests of inflow conditions for large-eddy simulation. Phys. Fluids 16 (12), 4696–4712.

Kim, Yusik, Castro, Ian P., Xie, Zheng-Tong, 2013. Divergence-free turbulence inflow conditions for large-eddy simulations with incompressible flow solvers. Comput. & Fluids 84, 56–68.

Lamberti, Giacomo, Amerio, Luca, Pomaranzi, Giulia, Zasso, Alberto, Gorlé, Catherine, 2020. Comparison of high resolution pressure measurements on a high-rise building in a closed and open-section wind tunnel. J. Wind Eng. Ind. Aerodyn. 204, 104247.

Lamberti, G., García-Sánchez, C., Sousa, J., Gorlé, C., 2018. Optimizing turbulent inflow conditions for large-eddy simulations of the atmospheric boundary layer. J. Wind Eng. Ind. Aerodyn. 177, 32–44.

Liu, Z., Prevatt, D.O., Aponte-Bermudez, L.D., Gurley, K.R., Reinhold, T.A., Akins, R.E., 2009. Field measurement and wind tunnel simulation of hurricane wind loads on a single family dwelling. Eng. Struct. 31 (10), 2265–2274.

Minor, J.E., 2005. Lessons learned from failures of the building envelope in windstorms. J. Archit. Eng. 11 (1), 10–13.

Morrison, M., Brown, T., Liu, Z., 2011. Comparison of field and full-scale laboratory peak pressures at the IBHS research center. In: Advances in Hurricane Engineering. pp. 1109–1124.

National Centers for Environmental Information (NCEI), NO.A.A., 2023. U.S. billion-dollar weather and climate disasters. http://dx.doi.org/10.25921/stkw-7w73, URL https://www.ncei.noaa.gov/access/billions/.

Okada, H., Ha, Y.-C., 1992. Comparison of wind tunnel and full-scale pressure measurement tests on the Texas Tech building. J. Wind Eng. Ind. Aerodyn. 43 (1), 1601–1612, URL https://www.sciencedirect.com/science/article/pii/016761059290375K. International Conference on Wind Engineering.

Ouyang, Z., Spence, S.M.J., 2019. A performance-based damage estimation framework for the building envelope of wind-excited engineered structures. J. Wind Eng. Ind. Aerodyn. 186, 139–154.

Paden, Ivan, García-Sánchez, Clara, Ledoux, Hugo, 2022. Towards automatic reconstruction of 3D city models tailored for urban flow simulations. Front. Built Environ. 8.

Pomaranzi, Giulia, Amerio, Luca, Schito, Paolo, Lamberti, Giacomo, Gorlé, Catherine, Zasso, Alberto, 2022. Wind tunnel pressure data analysis for peak cladding load estimation on a high-rise building. Journal of Wind Engineering and Industrial Aerodynamics 220, 104855.

Richardson, G.M., Hoxey, R.P., Robertson, A.P., Short, J.L., 1997. The Silsoe structures building: Comparisons of pressures measured at full scale and in two wind tunnels. J. Wind Eng. Ind. Aerodyn. 72, 187–197.

Richardson, G.M., Surry, D., 1991. Comparisons of wind-tunnel and full-scale surface pressure measurements on low-rise pitched-roof buildings. J. Wind Eng. Ind. Aerodyn. 38, 249–256.

Sparks, P.R., Schiff, S.D., Reinhold, T.A., 1994. Wind damage to envelopes of houses and consequent insurance losses. J. Wind Eng. Ind. Aerodyn. 53 (1–2), 145–155.

Tieleman, H.W., 2003. Wind tunnel simulation of wind loading on low-rise structures: A review. J. Wind Eng. Ind. Aerodyn. 91, 1627–1649.

Vreman, A.W., 2004. An eddy-viscosity subgrid-scale model for turbulent shear flow: Algebraic theory and applications. Phys. Fluids 16 (10), 3670–3681.

Williams, T., Kareem, A., 2003. Performance of building cladding in urban environments under extreme winds. In: Proceedings of the 11th International Conference on Wind Engineering, Lubbock. Vol. 7.

Xie, Zheng-Tong, Castro, Ian P., 2008. Efficient generation of inflow conditions for large-eddy simulation of street-scale flows. Flow Turbul. Combust. 81 (3), 449–470.